

## Article

# Thermal Decomposition of [AH][M(HCOO)<sub>3</sub>] Perovskite-Like Formates

Lilián Claudia Gómez-Aguirre <sup>1,\*</sup> , Jorge Otero-Canabal <sup>2</sup>, Manuel Sánchez-Andújar <sup>1</sup>,  
María Antonia Señaris-Rodríguez <sup>1</sup> , Socorro Castro-García <sup>1</sup>  and Breogán Pato-Doldán <sup>1,\*</sup> 

<sup>1</sup> QuiMolMat Group, Department of Chemistry, Faculty of Science and Advanced Scientific Research Center (CICA), University of A Coruña, Zapateira, 15071 A Coruña, Spain; msanchez@udc.es (M.S.-A.); m.senaris.rodriguez@udc.es (M.A.S.-R.); socorro.castro.garcia@udc.es (S.C.-G.)

<sup>2</sup> Molecular Spectroscopy Unit, SAI, University of A Coruña, 15071 A Coruña, Spain; jorge.otero@udc.es

\* Correspondence: claudia.gomez.aguirre@udc.es (L.C.G.-A.); breogan.pato@udc.es (B.P.-D.)

**Abstract:** A systematic study of the thermal decomposition of hybrid perovskites of formula [AH][M(HCOO)<sub>3</sub>] under inert atmosphere was performed by means of thermogravimetry and simultaneous infrared spectroscopy of the evolved gases. The influence of: (i) the metal ion of the [M(HCOO)<sub>3</sub>]<sup>−</sup> framework and (ii) the guest [AH]<sup>+</sup> cation, in the composition of the final residue was evaluated. In this work, it has been demonstrated that these materials can be used as precursors of metal or metal-oxide compounds—obtained free of carbon—, and that the composition of the final residue is determined by the standard reduction potential of the metal cation of the framework.

**Keywords:** coordination polymers; hybrid perovskites; thermolysis; formates



**Citation:** Gómez-Aguirre, L.C.; Otero-Canabal, J.; Sánchez-Andújar, M.; Señaris-Rodríguez, M.A.; Castro-García, S.; Pato-Doldán, B. Thermal Decomposition of [AH][M(HCOO)<sub>3</sub>] Perovskite-Like Formates. *Solids* **2021**, *2*, 165–176. <https://doi.org/10.3390/solids2020011>

Academic Editor: Guido Kickelbick

Received: 14 February 2021

Accepted: 4 April 2021

Published: 2 May 2021

**Publisher's Note:** MDPI stays neutral with regard to jurisdictional claims in published maps and institutional affiliations.



**Copyright:** © 2021 by the authors. Licensee MDPI, Basel, Switzerland. This article is an open access article distributed under the terms and conditions of the Creative Commons Attribution (CC BY) license (<https://creativecommons.org/licenses/by/4.0/>).

## 1. Introduction

Coordination polymers are hybrid inorganic/organic structures formed by metal cation centers that are linked by organic ligands, in the form of one-, two-, or three-dimensional crystalline structures. Moreover, guest molecules weakly bonded to the framework can be located inside the structure (see Figure 1, as an example).

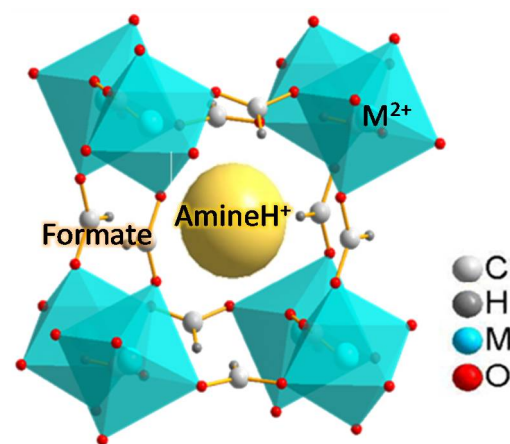


**Figure 1.** Conventional structure view of [AH][M(HCOO)<sub>3</sub>] perovskite. C atoms are in white, H in gray, M in light blue, O in red, and the guest amine AH<sup>+</sup> is in yellow.

The thermal stability of a coordination polymer is a key parameter which determines its optimal range for practical applications [1] including gas separation [2], ion exchange [3], water desalination [4], and moderate-temperature heat storage [5,6].

Beyond the thermal stability, understanding the decomposition process of coordination polymers opens new opportunities for their use as self-template precursors of highly

stable metal or metal oxide materials [7–11] with potential applications in catalysis [12], energy storage and conversion [13], supercapacitors [14], batteries, and fuel cells [15].

Usually, during the thermolysis of coordination polymers the guest molecules (if they exist) are the first ones being eliminated since they are weakly bonded to the framework. Afterwards, the framework collapses and the organic linkers are released as CO<sub>2</sub> or converted into a carbon matrix. The research in this field has been focused on the use of porous coordination polymers (also known as metal-organic frameworks, MOFs) thermally treated under inert conditions for the preparation of core-shell nanocomposites which consist in metal or metal oxide nanoparticles embedded in carbon porous nanostructures, respectively named M@C or MO@C [16,17]. However, for some applications (e.g., in magnetic or in piezoelectric devices), the carbon matrix can be more of a handicap than an asset. For these applications, it is worth looking for different coordination polymers formed by ligands of variable length to evaluate the possibility of obtaining metal (or metal oxide) products free of carbon.

In this context, the study of the thermal decomposition of coordination polymers with perovskite-type structures as potential self-template precursors of metal or metal oxide materials is of interest. Hybrid perovskites are some of the most studied covalent frameworks due to their interesting functional properties reported along the last two decades. Among them, compounds of the formula [AH][M(HCOO)<sub>3</sub>] (Figure 1) have attracted great interest due to their dielectric [18–20], magnetic [21,22], and multiferroic [23–26] properties.

Here, a systematic study of the degradation of the [AH][M(HCOO)<sub>3</sub>] crystalline materials containing different M<sup>2+</sup> cations, connected through formate (HCOO<sup>−</sup>) ligands, and hosting different protonated amines (AH<sup>+</sup>) is presented. The aim is to understand the decomposition mechanisms and the factors which determine their final residue.

## 2. Results

The thermal degradation of two groups of perovskite-like formates [AH][M(HCOO)<sub>3</sub>] was studied following the next strategy:

On one side, in order to evaluate the role of the metal cation on the thermal stability and degradation process, we compare a group of [CH<sub>3</sub>NH<sub>3</sub>][M(HCOO)<sub>3</sub>] perovskites containing the same methylammonium cation inside their cavities, and with different metal cations as part of the framework (M<sup>2+</sup> = Mg<sup>2+</sup>, Mn<sup>2+</sup>, Co<sup>2+</sup>, Ni<sup>2+</sup>, Cu<sup>2+</sup>, and Zn<sup>2+</sup>).

On the other side, in order to observe the effect of the guest ions (AH<sup>+</sup>) on the thermal degradation, we compare a series of Cd<sup>2+</sup> perovskites of formula [AH][Cd(HCOO)<sub>3</sub>] containing different amine cations inside their cavities (AH<sup>+</sup> = NH<sub>4</sub><sup>+</sup>, CH<sub>3</sub>NH<sub>3</sub><sup>+</sup>, and (CH<sub>3</sub>)<sub>2</sub>NH<sub>2</sub><sup>+</sup>).

### 2.1. Role of Metal Cations on the Thermal Decomposition of [CH<sub>3</sub>NH<sub>3</sub>][M(HCOO)<sub>3</sub>] Perovskites

Figure 2a shows the corresponding TGA curves for [CH<sub>3</sub>NH<sub>3</sub>][M(HCOO)<sub>3</sub>] compounds. TGA results reveal that these materials start to decompose between 150 °C (Cu<sup>2+</sup>) and 230 °C (Ni<sup>2+</sup>). The obtained residues after the complete thermal decomposition were analyzed by XRPD at room temperature. According to the XRPD results, the analyzed compounds can be divided in three groups in function of their final decomposition products: (i) M<sup>2+</sup> = Mg<sup>2+</sup>, Mn<sup>2+</sup>, and Zn<sup>2+</sup> formates decompose to the corresponding MO materials (Figures S1–S3 of ESI); (ii) M<sup>2+</sup> = Ni<sup>2+</sup> and Cu<sup>2+</sup> perovskites decompose to the pure M species (Figures S4 and S5); and (iii) Co<sup>2+</sup> compound decomposes to a mixture of 0.29 CoO + 0.71 Co (*w/w*) (Figure S6). These results are in agreement with those reported in the literature for anhydrous and dehydrate metal formates [27–30].

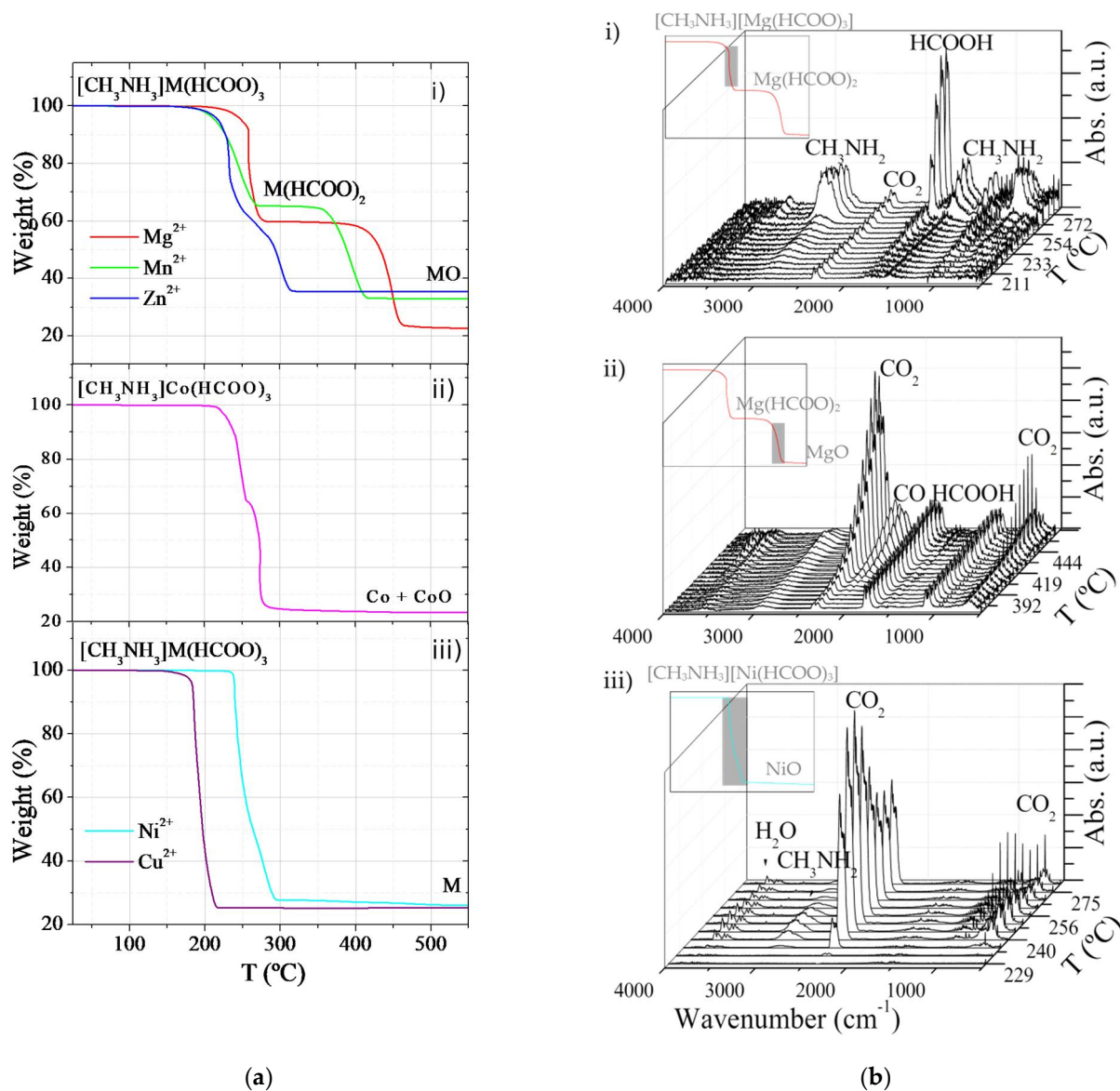


**Figure 2.** (a) Thermogravimetric analysis (TGA) curves of  $[\text{CH}_3\text{NH}_3][\text{M}(\text{HCOO})_3]$  where: (i)  $\text{M}^{2+} = \text{Mg}^{2+}$ ,  $\text{Mn}^{2+}$ , and  $\text{Zn}^{2+}$ ; (ii)  $\text{M}^{2+} = \text{Co}^{2+}$  and (iii)  $\text{M}^{2+} = \text{Ni}^{2+}$  and  $\text{Cu}^{2+}$ . (b) Infrared (IR) spectra of released gases from  $[\text{CH}_3\text{NH}_3][\text{M}(\text{HCOO})_3]$  compounds at different temperatures: (i)  $[\text{CH}_3\text{NH}_3][\text{Mg}(\text{HCOO})_3]$  between 200 and 280 °C, (ii)  $[\text{CH}_3\text{NH}_3][\text{Mg}(\text{HCOO})_3]$  between 370 and 470 °C, and (iii)  $[\text{CH}_3\text{NH}_3][\text{Ni}(\text{HCOO})_3]$  between 208 and 280 °C. Insets: the temperature range (in gray) of the IR experiments in the thermogravimetric (TG) curves.

Additionally, the wide range of thermal stability showed by the intermediate degradation compounds of  $[\text{CH}_3\text{NH}_3][\text{Mg}(\text{HCOO})_3]$  (280–370 °C) and  $[\text{CH}_3\text{NH}_3][\text{Mn}(\text{HCOO})_3]$  (280–340 °C), allowed for their isolation and identification as  $\text{Mg}(\text{HCOO})_2$  and  $\text{Mn}(\text{HCOO})_2$  (Figures S7 and S8).

Table 1 recompiles the most relevant information obtained by TGA and XRPD relative to the thermal decomposition of this group of compounds.

**Table 1.** Summary of the thermal decomposition of  $[\text{CH}_3\text{NH}_3][\text{M}(\text{HCOO})_3]$  compounds.

| $\text{M}^{2+}$  | Step | T (°C)  | Weight Loss (%) |       | Product                          |
|------------------|------|---------|-----------------|-------|----------------------------------|
|                  |      |         | Exp.            | Calc. |                                  |
| $\text{Mg}^{2+}$ | 1    | 200–280 | 40.4            | 40.3  | $\text{Mg}(\text{HCOO})_2$       |
|                  | 2    | 370–470 | 35.7            | 38.7  | $\text{MgO}$                     |
| $\text{Mn}^{2+}$ | 1    | 180–280 | 34.8            | 34.7  | $\text{Mn}(\text{HCOO})_2$       |
|                  | 2    | 340–423 | 32.3            | 33.3  | $\text{MnO}$                     |
| $\text{Co}^{2+}$ | 1    | 215–254 | 33.8            | 34.1  | $\text{Co}(\text{HCOO})_2^*$     |
|                  | 2    | 254–290 | 41.1            | 37.8  | $0.29\text{Co} + 0.71\text{CoO}$ |
| $\text{Ni}^{2+}$ | 1    | 230–280 | 72.2            | 74.0  | $\text{Ni}$                      |
| $\text{Cu}^{2+}$ | 1    | 150–220 | 74.3            | 72.2  | $\text{Cu}$                      |
| $\text{Zn}^{2+}$ | 1    | 160–240 | 32.8            | 33.2  | $\text{Zn}(\text{HCOO})_2^*$     |
|                  | 2    | 240–320 | 32.0            | 31.8  | $\text{ZnO}$                     |

\* no isolated.

To deep further into the mechanism of the observed thermal decomposition for these compounds, the released gases were analyzed by infrared spectroscopy. The IR spectra obtained at different temperatures was compared against the reference spectra from the National Institute of Standards and Technology (NIST) database [31]. The corresponding IR spectra are shown in Figures 2b and S9–S18.

$[\text{CH}_3\text{NH}_3][\text{Mg}(\text{HCOO})_3]$  is stable up to 200 °C, and above this temperature it shows a two-step degradation process, until it finally decomposes into  $\text{MgO}$  (Figure S1). During the first decomposition step (200–280 °C) it degrades to the  $\text{Mg}(\text{HCOO})_2$  intermediate (Figure S7), releasing  $\text{CH}_3\text{NH}_2$  and  $\text{HCOOH}$  as the main gases, together with a minor portion of  $\text{CO}_2$  (Figures 2b(i) and S9). In the second step (370–470 °C), the intermediate decomposes eliminating  $\text{CO}_2$  together with some  $\text{CO}$  and  $\text{HCOOH}$  (Figures 2b(ii) and S10).

$[\text{CH}_3\text{NH}_3][\text{Mn}(\text{HCOO})_3]$  is stable up to 180 °C and then it decomposes into a two-step process until it finally yields  $\text{MnO}$  (Figure S2). The main gases released during the first-step of decomposition are  $\text{CH}_3\text{NH}_2$ ,  $\text{CO}_2$ , and  $\text{HCOOH}$  (Figure S11). The intermediate  $\text{Mn}(\text{HCOO})_2$  (Figure S8) degrades by releasing  $\text{CO}_2$ ,  $\text{CO}$ , and  $\text{H}_2\text{O}$  (Figure S12).

$[\text{CH}_3\text{NH}_3][\text{Zn}(\text{HCOO})_3]$  is stable up to 160 °C. It degrades in a smooth two-step process to  $\text{ZnO}$  (Figure S3). The decomposition starts with the releasing of  $\text{CO}_2$  together with  $\text{CH}_3\text{NH}_2$  and  $\text{H}_2\text{O}$ . The amine is eliminated through the whole degradation process. Above 240 °C, the formate linkers are removed or degraded not only as  $\text{CO}_2$  but also as  $\text{HCOOH}$ ,  $\text{CO}$ , and  $\text{H}_2\text{O}$  (Figures S13 and S14).

$[\text{CH}_3\text{NH}_3][\text{Co}(\text{HCOO})_3]$  is stable up to 215 °C. This  $\text{Co}^{2+}$  compound degrades in a smooth two-step process to  $\text{Co}$  (71.1%) mixed with  $\text{CoO}$  (28.9%) (Figure S6).  $\text{CO}_2$  is the main gas observed from the beginning and up to the end of the degradation process (steps 1 and 2). During the first degradation step  $\text{CH}_3\text{NH}_2$  and  $\text{H}_2\text{O}$  are observed, while  $\text{CH}_3\text{NH}_2$ ,  $\text{H}_2\text{O}$ , and  $\text{CO}$  are detected during the second step (Figures S15 and S16).

$[\text{CH}_3\text{NH}_3][\text{Ni}(\text{HCOO})_3]$  and  $[\text{CH}_3\text{NH}_3][\text{Cu}(\text{HCOO})_3]$  show a similar single-step degradation process. The  $\text{Ni}^{2+}$  material is stable up to 230 °C and the  $\text{Cu}^{2+}$  one up to 150 °C. The two compounds decompose to pure  $\text{Ni}$  (Figure S4) and  $\text{Cu}$  (Figure S5) by releasing  $\text{CO}_2$  together with  $\text{CH}_3\text{NH}_2$  and  $\text{H}_2\text{O}$  during the whole degradation processes (Figures 2b(iii), S17 and S18).

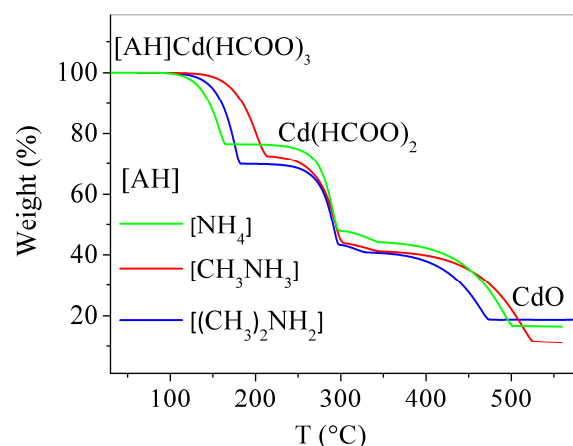
Table 2 contains a list of the volatile species observed at the different decomposition steps of the  $[\text{CH}_3\text{NH}_3][\text{M}(\text{HCOO})_3]$  compounds. The gases from the second step are in agreement with gases reported by Shishido and Masuda for the anhydrous formates [32].

**Table 2.** Released gases at different decomposition steps of  $[\text{CH}_3\text{NH}_3][\text{M}(\text{HCOO})_3]$  materials.

| $\text{M}^{2+}$  | Step No. | Main Released Gases  |
|------------------|----------|--|
| $\text{Mg}^{2+}$ | 1        | $\text{CH}_3\text{NH}_2$ , $\text{HCOOH}$ , $\text{CO}_2$                                      |
|                  | 2        | $\text{CO}_2$ , $\text{CO}$ , $\text{HCOOH}$   |
| $\text{Mn}^{2+}$ | 1        | $\text{CH}_3\text{NH}_2$ , $\text{CO}_2$ , $\text{HCOOH}$                                      |
|                  | 2        | $\text{CO}_2$ , $\text{CO}$ , $\text{H}_2\text{O}$   |
| $\text{Zn}^{2+}$ | 1        | $\text{CH}_3\text{NH}_2$ , $\text{CO}_2$ , $\text{H}_2\text{O}$                                |
|                  | 2        | $\text{CH}_3\text{NH}_2$ , $\text{CO}_2$ , $\text{CO}$ , $\text{HCOOH}$ , $\text{H}_2\text{O}$ |
| $\text{Co}^{2+}$ | 1        | $\text{CO}_2$ , $\text{CH}_3\text{NH}_2$ , $\text{H}_2\text{O}$                                |
|                  | 2        | $\text{CH}_3\text{NH}_2$ , $\text{CO}_2$ , $\text{H}_2\text{O}$ , $\text{CO}$                  |
| $\text{Ni}^{2+}$ | 1        | $\text{CH}_3\text{NH}_2$ , $\text{CO}_2$ , $\text{H}_2\text{O}$                                |
| $\text{Cu}^{2+}$ | 1        | $\text{CH}_3\text{NH}_2$ , $\text{CO}_2$ , $\text{H}_2\text{O}$                                |

## 2.2. Role of A-Site Cation on the Thermal Decomposition of $[\text{AH}][\text{Cd}(\text{HCOO})_3]$ Materials

Figure 3 shows the corresponding TGA curves for  $[\text{AH}][\text{Cd}(\text{HCOO})_3]$  compounds. Table S2 shows a summary of the thermal decomposition results for these compounds.

**Figure 3.** TGA curves of  $[\text{AH}][\text{Cd}(\text{HCOO})_3]$  where  $\text{AH}^+ = \text{NH}_4^+$ ,  $\text{CH}_3\text{NH}_3^+$ , and  $(\text{CH}_3)_2\text{NH}_3^+$ .

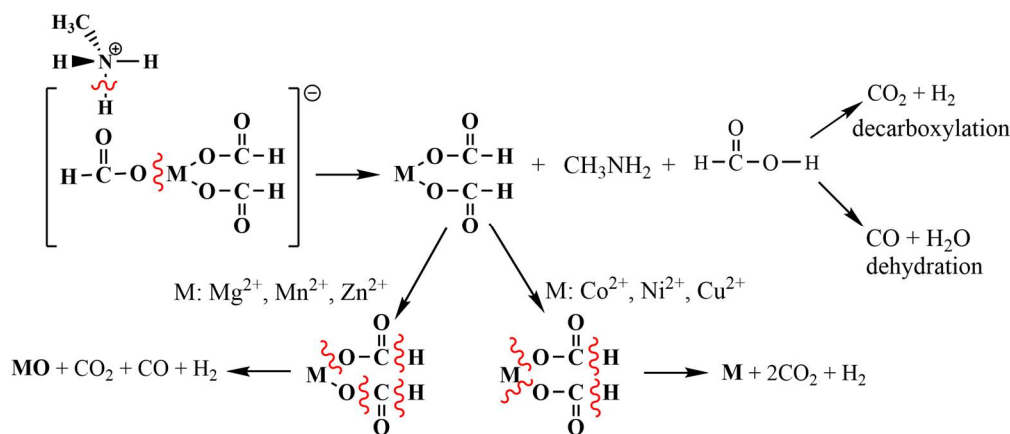
$[\text{AH}][\text{Cd}(\text{HCOO})_3]$  compounds, with  $\text{AH}^+ = \text{NH}_4^+$ ,  $\text{CH}_3\text{NH}_3^+$ , and  $(\text{CH}_3)_2\text{NH}_2^+$  guest cations, degrade in a four-step process. According to the IR spectra of the released gases (Figures S20–S24), the amine is released during the first decomposition step together with a formate group of the framework as  $\text{HCOOH}$  and/or  $\text{CO}_2$ .

For  $[\text{NH}_4][\text{Cd}(\text{HCOO})_3]$ , the wide range of thermal stability showed by the intermediate compound formed at 200 °C, allowed its identification by XRPD as  $0.65 \text{ Cd}(\text{HCOO})_2 + 0.35 \text{ Cd}(\text{HCOO})_2 \cdot 2\text{H}_2\text{O}$  (*w/w*) (Figure S25).

The decomposition of the intermediate  $\text{Cd}(\text{HCOO})_2$  compound has been described elsewhere by Małecka and co-workers [33].  $\text{Cd}(\text{HCOO})_2$  decomposes through the formation of an oxalate anion ( $\text{C}_2\text{O}_4^{2-}$ ) which further evolves to the carbonate [27]. The presence of  $\text{CdCO}_3$  was confirmed by XRPD on the residue left by  $[\text{CH}_3\text{NH}_3][\text{Cd}(\text{HCOO})_3]$  decomposition (Figure S19) at 600 °C. The XRPD analyses show that  $[\text{CH}_3\text{NH}_3][\text{Cd}(\text{HCOO})_3]$  degrades to  $0.69 \text{ CdCO}_3 + 0.31 \text{ CdO}$  (*w/w*). This result is in agreement with the ones observed for the decomposition of  $\text{Cd}(\text{HCOO})_2$  to  $\text{CdCO}_3$  [33] and of  $\text{Cd}(\text{HCOO})_2 \cdot 2\text{H}_2\text{O}$  to  $\text{Cd}$  (sublimed)/ $\text{CdO}$  [27].

### 3. Discussion

The obtained results have allowed us to determine the decomposition mechanism for  $[\text{CH}_3\text{NH}_3][\text{M}(\text{HCOO})_3]$  and  $[\text{AH}][\text{Cd}(\text{HCOO})_3]$  compounds. The proposed degradation for  $[\text{CH}_3\text{NH}_3][\text{M}(\text{HCOO})_3]$  is summarized in Scheme 1. In these compounds, the decomposition starts with the elimination of the  $\text{CH}_3\text{NH}_3^+$  cations which are linked to the anionic  $[\text{M}(\text{HCOO})_3]^-$  framework presumably through hydrogen bonds. The framework is no longer stable and one of the formate  $\text{HCOO}^-$  groups is also released. By H-transfer between the  $\text{HCOO}^-$  and  $\text{CH}_3\text{NH}_3^+$  species,  $\text{CH}_3\text{NH}_2$  and  $\text{HCOOH}$  are obtained as gas products. Formic acid ( $\text{HCOOH}$ ) can decompose following two different possible mechanisms, decarboxylation ( $\text{CO}_2 + \text{H}_2$ ) and dehydration ( $\text{CO} + \text{H}_2\text{O}$ ) [34].



**Scheme 1.** Thermal degradation of the  $[\text{CH}_3\text{NH}_3][\text{M}(\text{HCOO})_3]$  compounds, where  $\text{M}^{2+} = \text{Mg}^{2+}, \text{Mn}^{2+}, \text{Co}^{2+}, \text{Ni}^{2+}, \text{Cu}^{2+}$ , and  $\text{Zn}^{2+}$ . Solid species, characterized by XRPD, are represented in bold.

For the  $[\text{CH}_3\text{NH}_3][\text{M}(\text{HCOO})_3]$  compounds, the intermediate  $\text{M}(\text{HCOO})_2$ , isolated for  $\text{M}^{2+} = \text{Mg}^{2+}$  and  $\text{Mn}^{2+}$ , decomposes releasing  $\text{CO}_2$ ,  $\text{CO}$ , and  $\text{HCOOH}$  (Table 2 and IR Figures on the ESI). The formation of these species can be explained by the rupture of M–O and C–O bonds of the intermediate units.

From the systematic study here reported for  $[\text{CH}_3\text{NH}_3][\text{M}(\text{HCOO})_3]$ , we have elucidated that the  $\text{M}^{2+}$  cation of the covalent bonded framework plays a crucial role on the degradation pathway, which can occur through two different routes: one corresponding to MO oxides and a second one corresponding to pure M metal. In particular,  $\text{Mg}^{2+}$ ,  $\text{Mn}^{2+}$ ,  $\text{Zn}^{2+}$ , and  $\text{Cd}^{2+}$  compounds degrade to the corresponding MO oxides, while  $\text{Co}^{2+}$ ,  $\text{Ni}^{2+}$ , and  $\text{Cu}^{2+}$  compounds are reduced to the respective pure M species.

Very interestingly, we have determined that there is a direct correlation/link between the observed route and the standard reduction potential of the metal cation of the framework (Figure 4). Metal cations with a standard reduction potential of  $-0.27$  V or higher ( $-0.27$  V for  $\text{Co}^{2+}$ ,  $-0.23$  V for  $\text{Ni}^{2+}$ , and  $0.34$  V for  $\text{Cu}^{2+}$ ) are reduced to pure metal species, whereas metal cations with a standard reduction potential lower than  $-0.27$  V ( $-0.40$  V for  $\text{Cd}^{2+}$ ,  $-0.76$  V for  $\text{Zn}^{2+}$ ,  $-1.18$  V for  $\text{Mn}^{2+}$ , and  $-2.37$  V for  $\text{Mg}^{2+}$ ) are not reduced to zero oxidation state, but tend to combine with the oxygen from the ligands to yield the metal oxides.

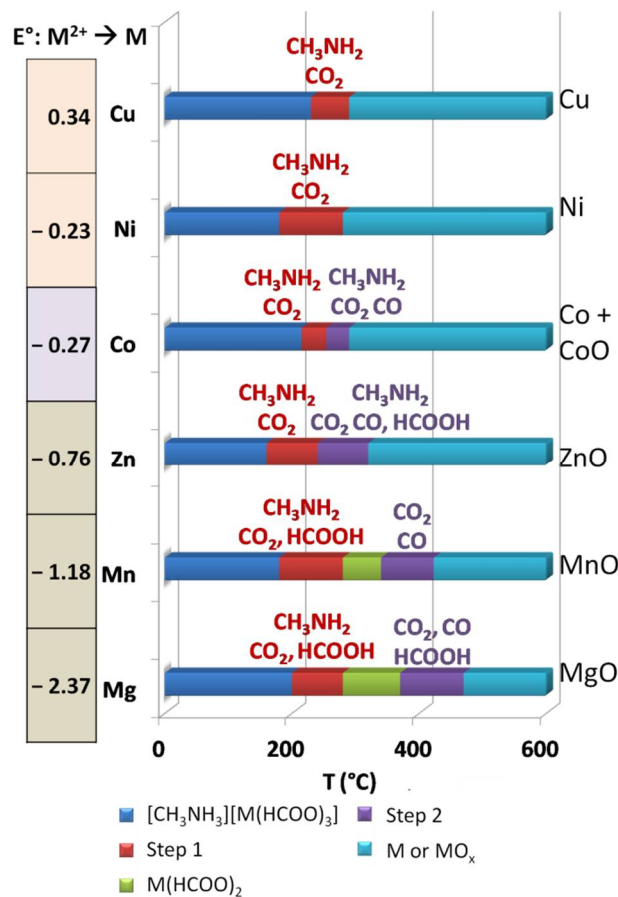


**Figure 4.** Diagram showing the stability range of several perovskite-like formates.

The presence of CoO as the minor phase (28.9%) of decomposition of  $[\text{CH}_3\text{NH}_3][\text{Co}(\text{HCOO})_3]$  could be related with the fact that  $\text{Co}^{2+}$  has a standard potential value of  $-0.27$  V, which coincides with the limit potential that determines if the reduction product is favoured.

In addition, it has been observed that lower reduction potentials sequentially stabilize the intermediate  $\text{M}(\text{HCOO})_2$ , so that  $\text{Cu}^{2+}$ - and  $\text{Ni}^{2+}$ -compounds show only one degradation step,  $\text{Co}^{2+}$ - and  $\text{Zn}^{2+}$ -compounds show two degradation steps and finally the  $\text{M}(\text{HCOO})_2$  species can be isolated for  $\text{Mg}^{2+}$ - and  $\text{Mn}^{2+}$ -materials (Figure 4).

It is worth noting that these results are in agreement with the ones observed by Das for porous coordination polymers (MOFs) containing elongated organic linkers [35], whose decomposition gives rise to porous  $\text{M@C}$  nanocomposites, and porous  $\text{MO@C}$  nanocomposites [12]. In a subsequent review, Gascon and co-workers, rationalized that in those MOFs yielding metal species by thermolysis, the carbon matrix (obtained as by-product) acts as the reducing agent (through the  $\text{C} \rightarrow \text{CO}_2$  conversion) [12]. In contrast, for the compounds presented here,  $[\text{AH}][\text{M}(\text{HCOO})_3]$ , no carbon matrix is produced during the decomposition. We propose that for  $[\text{CH}_3\text{NH}_3][\text{M}(\text{HCOO})_3]$  where  $\text{M}^{2+} = \text{Co}^{2+}$ ,  $\text{Ni}^{2+}$ , and  $\text{Cu}^{2+}$ , the formate ( $\text{HCOO}^-$ ) ligand is acting as a reducing agent as follows (Scheme 2):



**Scheme 2.** Proposed redox reaction occurring on  $[\text{CH}_3\text{NH}_3][\text{M}(\text{HCOO})_3]$  where  $\text{M}^{2+} = \text{Co}^{2+}$ ,  $\text{Ni}^{2+}$ , and  $\text{Cu}^{2+}$ .

In an inert atmosphere and above the decomposition temperature, the Gibbs free energy/reduction potential represented on the Ellingham diagram predicts the metallic species/metal oxides which are favoured.



#### 4. Materials and Methods

Synthesis:  $[\text{CH}_3\text{NH}_3][\text{M}(\text{HCOO})_3]$  materials, where  $\text{M}^{2+} = \text{Mg}^{2+}, \text{Mn}^{2+}, \text{Co}^{2+}, \text{Ni}^{2+}, \text{Cu}^{2+}$ , and  $\text{Zn}^{2+}$ , and  $[\text{AH}][\text{Cd}(\text{HCOO})_3]$  materials, where  $\text{AH}^+ = \text{NH}_4^+, \text{CH}_3\text{NH}_3^+$ , and  $(\text{CH}_3)_2\text{NH}_2^+$ , were synthesized under solvothermal conditions followed by the slow evaporation of the mother liquor [21], or by slow diffusion method [36]. Table S1 of supplementary materials summarizes the list and quality of the starting reagents.

Thermal Studies: Thermogravimetric analyses (TGAs) were carried out in a SDT2960 TGA-DTA from TA Instruments (Waters Corporation, Milford, Massachusetts, USA). For these experiments, approximately 27 mg of each sample were heated at a rate of 5 K/min from room temperature to 600 °C using corundum crucibles under a flow of dry nitrogen. The TGA instrument was coupled to a Fourier transform infrared (FT-IR) spectrometer Bruker VECTOR22 working over the wavenumber range from 400 to 4000  $\text{cm}^{-1}$ .

X-Ray Powder Diffraction: (XRPD) was performed in a Siemens D-5000 diffractometer at room temperature using  $\text{CuK}\alpha$  radiation ( $\lambda = 1.5418 \text{ \AA}$ ). XRPD patterns were refined by the Rietveld method using the software X'Pert HighScore Plus. The background was fitted with a Chebyshev function with 6 terms. The peak profiles were modelled using a pseudo-Voigt function. The cell parameters, the phase fraction, and the zero shift were also refined.

#### 5. Conclusions

The exothermic decomposition of  $[\text{AH}][\text{M}(\text{HCOO})_3]$  perovskite-like coordination polymers under inert atmosphere takes place in a single- or multi-step process to the corresponding MO or M residue. The composition of the final residue is determined by the standard reduction potential of the metal in the framework. This means that these coordination polymers can be used as self-templates precursors, and that it is possible to predict if the metal or the metal oxide will be obtained.

In contrast with the decomposition of coordination polymers containing long C-rich organic ligands (MOFs), thermolysis of perovskite-like coordination polymers provides a clean and direct method towards the synthesis of metal oxides and metals, avoiding the production of a carbon matrix or other impurities that are not desired for specific applications.

**Supplementary Materials:** The following are available online at <https://www.mdpi.com/article/10.3390/solids2020011/s1>, Table S1: Quality of reagents used in the synthesis of  $[\text{AH}][\text{M}(\text{HCOO})_3]$  materials, Figure S1: XRPD pattern obtained after heating the  $[\text{CH}_3\text{NH}_3][\text{Mg}(\text{HCOO})_3]$  sample to 600 °C. Comparison against the trace reported in the literature for MgO [37], Figure S2: XRPD pattern obtained after heating the  $[\text{CH}_3\text{NH}_3][\text{Mn}(\text{HCOO})_3]$  sample to 600 °C. Comparison against the trace reported in the literature for MnO [37], Figure S3: XRPD pattern obtained after heating the  $[\text{CH}_3\text{NH}_3][\text{Zn}(\text{HCOO})_3]$  sample to 600 °C. Comparison against the trace reported in the literature for ZnO [38], Figure S4: XRPD pattern obtained after heating the  $[\text{CH}_3\text{NH}_3][\text{Ni}(\text{HCOO})_3]$  sample to 600 °C. Comparison against the trace reported in the literature for Ni [39], Figure S5: XRPD pattern obtained after heating the  $[\text{CH}_3\text{NH}_3][\text{Cu}(\text{HCOO})_3]$  sample to 600 °C. Comparison against the trace reported in the literature for Cu [40], Figure S6: Rietveld refinement of the XRPD pattern obtained after heating the  $[\text{CH}_3\text{NH}_3][\text{Co}(\text{HCOO})_3]$  sample to 600 °C. Literature source for CoO [37] and Co [41]. Figure S7: Rietveld refinement of the XRPD pattern obtained after heating the  $[\text{CH}_3\text{NH}_3][\text{Mg}(\text{HCOO})_3]$  sample to 350 °C. Literature source for  $\beta\text{-Mg}(\text{HCOO})_2$  [42], Figure S8: Rietveld refinement of the XRPD pattern obtained after heating the  $[\text{CH}_3\text{NH}_3][\text{Mn}(\text{HCOO})_3]$  sample to 300 °C. Literature source for  $\text{Mn}(\text{HCOO})_2 \cdot 2\text{H}_2\text{O}$  [43], Figure S8: IR spectra of released gases from  $[\text{CH}_3\text{NH}_3][\text{Mg}(\text{HCOO})_3]$  between 200 and 280 °C, Figure S9: IR spectra of released gases from  $[\text{CH}_3\text{NH}_3][\text{Mg}(\text{HCOO})_3]$  between 370 and 470 °C, Figure S10: IR spectra of released gases from  $[\text{CH}_3\text{NH}_3][\text{Mg}(\text{HCOO})_3]$  between 370 and 470 °C, Figure S11: IR spectra of released gases from  $[\text{CH}_3\text{NH}_3][\text{Mn}(\text{HCOO})_3]$  between 180 and 280 °C, Figure S12: IR spectra of released gases from  $[\text{CH}_3\text{NH}_3][\text{Mn}(\text{HCOO})_3]$  between 340 and 423 °C, Figure S13: IR spectra of released gases from  $[\text{CH}_3\text{NH}_3][\text{Zn}(\text{HCOO})_3]$  between 160 and 240 °C, Figure S14: IR spectra of released gases from  $[\text{CH}_3\text{NH}_3][\text{Zn}(\text{HCOO})_3]$  between 240 and 320 °C, Figure S15: IR spectra of released gases from  $[\text{CH}_3\text{NH}_3][\text{Co}(\text{HCOO})_3]$  between 215 and 254 °C, Figure S16: IR spectra of released gases

from  $[\text{CH}_3\text{NH}_3][\text{Co}(\text{HCOO})_3]$  between 254 and 290 °C, Figure S17: IR spectra of released gases from  $[\text{CH}_3\text{NH}_3][\text{Ni}(\text{HCOO})_3]$  between 200 and 280 °C, recorded at 2 K/min, Figure S18: IR spectra of released gases from  $[\text{CH}_3\text{NH}_3][\text{Cu}(\text{HCOO})_3]$  between 170 and 220 °C, Table S2: Summary of the thermal decomposition of  $[\text{AH}][\text{Cd}(\text{HCOO})_3]$  compounds, Figure S19: Rietveld refinement of the XRPD pattern obtained after heating the  $[\text{CH}_3\text{NH}_3][\text{Cd}(\text{HCOO})_3]$  sample to 600 °C. Literature source for  $\text{CdCO}_3$  [44] and  $\text{CdO}$  [45], Figure S20: IR spectra of released gases from  $[\text{NH}_4][\text{Cd}(\text{HCOO})_3]$  between 100 and 166 °C, Figure S21: IR spectra of released gases from  $[\text{NH}_4][\text{Cd}(\text{HCOO})_3]$  between 210 and 290 °C, Figure S22: IR spectra of released gases from  $[(\text{CH}_3)_2\text{NH}_2][\text{Cd}(\text{HCOO})_3]$  between 120 and 200 °C, Figure S23: IR spectra of released gases from  $[(\text{CH}_3)_2\text{NH}_2][\text{Cd}(\text{HCOO})_3]$  between 250 and 296 °C, Figure S24: IR spectra of released gases from  $[(\text{CH}_3)_2\text{NH}_2][\text{Cd}(\text{HCOO})_3]$  between 306 and 352 °C, Figure S25: Rietveld refinement of the XRPD pattern obtained after heating the  $[\text{NH}_4][\text{Cd}(\text{HCOO})_3]$  sample to 200 °C. Literature source for  $\text{Cd}(\text{HCOO})_3 \cdot 2\text{H}_2\text{O}$  [46] and  $\text{Cd}(\text{HCOO})_2$  [47].

**Author Contributions:** Conceptualization, L.C.G.-A. and B.P.-D.; methodology, L.C.G.-A., B.P.-D. and J.O.-C.; formal analysis, L.C.G.-A., B.P.-D. and J.O.-C.; investigation, L.C.G.-A. and B.P.-D.; resources, S.C.-G., M.S.-A. and M.A.S.-R.; writing—original draft preparation, L.C.G.-A. and B.P.-D.; writing—review and editing, L.C.G.-A., B.P.-D., S.C.-G., M.S.-A. and M.A.S.-R.; project administration, S.C.-G., M.S.-A. and M.A.S.-R.; funding acquisition, S.C.-G., M.S.-A. and M.A.S.-R. All authors have read and agreed to the published version of the manuscript.

**Funding:** This research was funded by Ministerio de Economía y Competitividad MINECO (Spain), grant number FEDER MAT2010-21342-C02-01 and by Xunta de Galicia (Spain), grant number PGIDIT10PXB103272PR.

**Data Availability Statement:** The datasets generated and analysed during the current study are available from the corresponding author on reasonable request.

**Acknowledgments:** Authors want to thank the people in charge of the development and maintenance of the Crystallographic Open Database [48], The American Mineralogist Crystal Structure database [49] and The NIST Chemistry WebBook [50].

**Conflicts of Interest:** The authors declare no conflict of interest.

## References

1. Howarth, A.J.; Liu, Y.; Li, P.; Li, Z.; Wang, T.C.; Hupp, J.T.; Farha, O.K. Chemical, thermal and mechanical stabilities of metal-organic frameworks. *Nat. Rev. Mater.* **2016**, *1*, 1–15. [[CrossRef](#)]
2. Li, J.R.; Kuppler, R.J.; Zhou, H.C. Selective gas adsorption and separation in metal-organic frameworks. *Chem. Soc. Rev.* **2009**, *38*, 1477–1504. [[CrossRef](#)]
3. Zhao, X.; Bu, X.; Wu, T.; Zheng, S.T.; Wang, L.; Feng, P. Selective anion exchange with nanogated isoreticular positive metal-organic frameworks. *Nat. Commun.* **2013**, *4*, 2344. [[CrossRef](#)] [[PubMed](#)]
4. Liu, X.; Demir, N.K.; Wu, Z.; Li, K. Highly Water-Stable Zirconium Metal-Organic Framework UiO-66 Membranes Supported on Alumina Hollow Fibers for Desalination. *J. Am. Chem. Soc.* **2015**, *137*, 6999–7002. [[CrossRef](#)] [[PubMed](#)]
5. Henninger, S.K.; Habib, H.A.; Janiak, C. MOFs as adsorbents for low temperature heating and cooling applications. *J. Am. Chem. Soc.* **2009**, *131*, 2776–2777. [[CrossRef](#)]
6. Cadiau, A.; Lee, J.S.; Damasceno Borges, D.; Fabry, P.; Devic, T.; Wharmby, M.T.; Martineau, C.; Foucher, D.; Taulelle, F.; Jun, C.H.; et al. Design of Hydrophilic Metal Organic Framework Water Adsorbents for Heat Reallocation. *Adv. Mater.* **2015**, *27*, 4775–4780. [[CrossRef](#)] [[PubMed](#)]
7. Peng, L.; Zhang, J.; Xue, Z.; Han, B.; Li, J.; Yang, G. Large-pore mesoporous  $\text{Mn}_3\text{O}_4$  crystals derived from metal-organic frameworks. *Chem. Commun.* **2013**, *49*, 11695–11697. [[CrossRef](#)] [[PubMed](#)]
8. Cho, W.; Park, S.; Oh, M. Coordination polymer nanorods of Fe-MIL-88B and their utilization for selective preparation of hematite and magnetite nanorods. *Chem. Commun.* **2011**, *47*, 4138–4140. [[CrossRef](#)]
9. Li, J.; Xia, W.; Tang, J.; Tan, H.; Wang, J.; Kaneti, Y.V.; Bando, Y.; Wang, T.; He, J.; Yamauchi, Y. MOF nanoleaves as new sacrificial templates for the fabrication of nanoporous Co-N:X/C electrocatalysts for oxygen reduction. *Nanoscale Horiz.* **2019**, *4*, 1006–1013. [[CrossRef](#)]
10. Song, Y.; Li, X.; Sun, L.; Wang, L. Metal/metal oxide nanostructures derived from metal-organic frameworks. *RSC Adv.* **2015**, *5*, 7267–7279. [[CrossRef](#)]
11. Gómez-Aguirre, L.C.; Castro-García, S.; Sánchez-Andújar, M.; Yáñez-Vilar, S.; Mira, J.; Bermúdez-García, J.M.; Centeno, T.A.; Señaris-Rodríguez, M.A. A Facile Synthesis of  $\text{Co}_3\text{O}_4$  Hollow Microtubes by Decomposition of a Cobalt Metal-Organic Framework. *Eur. J. Inorg. Chem.* **2016**, *2016*, 4463–4469. [[CrossRef](#)]

12. Oar-Arteta, L.; Wezendonk, T.; Sun, X.; Kapteijn, F.; Gascon, J. Metal organic frameworks as precursors for the manufacture of advanced catalytic materials. *Mater. Chem. Front.* **2017**, *1*, 1709–1745. [[CrossRef](#)]
13. Sun, J.K.; Xu, Q. Functional materials derived from open framework templates/precursors: Synthesis and applications. *Energy Environ. Sci.* **2014**, *7*, 2071–2100. [[CrossRef](#)]
14. Ansari, S.N.; Saraf, M.; Gupta, A.K.; Mobin, S.M. Functionalized Cu-MOF@CNT Hybrid: Synthesis, Crystal Structure and Applicability in Supercapacitors. *Chem. Asian J.* **2019**, *14*, 3566–3571. [[CrossRef](#)]
15. Zhao, Y.; Song, Z.; Li, X.; Sun, Q.; Cheng, N.; Lawes, S.; Sun, X. Metal organic frameworks for energy storage and conversion. *Energy Storage Mater.* **2016**, *2*, 35–62. [[CrossRef](#)]
16. Liu, B.; Shioyama, H.; Akita, T.; Xu, Q. Metal-organic framework as a template for porous carbon synthesis. *J. Am. Chem. Soc.* **2008**, *130*, 5390–5391. [[CrossRef](#)] [[PubMed](#)]
17. Wang, J.; Wang, Y.; Hu, H.; Yang, Q.; Cai, J. From metal-organic frameworks to porous carbon materials: Recent progress and prospects from energy and environmental perspectives. *Nanoscale* **2020**, *12*, 4238–4268. [[CrossRef](#)]
18. Jain, P.; Dalal, N.S.; Toby, B.H.; Kroto, H.W.; Cheetham, A.K. Order-disorder antiferroelectric phase transition in a hybrid inorganic-organic framework with the perovskite architecture. *J. Am. Chem. Soc.* **2008**, *130*, 10450–10451. [[CrossRef](#)] [[PubMed](#)]
19. Sánchez-Andújar, M.; Presedo, S.; Yáñez-Vilar, S.; Castro-García, S.; Shamir, J.; Señaris-Rodríguez, M.A. Characterization of the order-disorder dielectric transition in the hybrid organic-inorganic perovskite-like formate Mn(HCOO)3[(CH3)2NH2]. *Inorg. Chem.* **2010**, *49*, 1510–1516. [[CrossRef](#)]
20. Pato-Doldán, B.; Sánchez-Andújar, M.; Gómez-Aguirre, L.C.; Yáñez-Vilar, S.; López-Beceiro, J.; Gracia-Fernández, C.; Haghighirad, A.A.; Ritter, F.; Castro-García, S.; Señaris-Rodríguez, M.A. Near room temperature dielectric transition in the perovskite formate framework [(CH3)2NH2][Mg(HCOO)3]. *Phys. Chem. Chem. Phys.* **2012**, *14*, 8498–8501. [[CrossRef](#)]
21. Pato-Doldán, B.; Gómez-Aguirre, L.C.; Hansen, A.P.; Mira, J.; Castro-García, S.; Sánchez-Andújar, M.; Señaris-Rodríguez, M.A.; Zapf, V.S.; Singleton, J. Magnetic transitions and isotropic: Versus anisotropic magnetic behaviour of [CH3NH3][M(HCOO)3] M = Mn<sup>2+</sup>, Co<sup>2+</sup>, Ni<sup>2+</sup>, Cu<sup>2+</sup> metal-organic perovskites. *J. Mater. Chem. C* **2016**, *4*, 11164–11172. [[CrossRef](#)]
22. Hu, K.-L.; Kurmoo, M.; Wang, Z.; Gao, S. Metal-organic perovskites: Synthesis, structures, and magnetic properties of [C(NH2)3][M(II)(HCOO)3] (M = Mn, Fe, Co, Ni, Cu, and Zn; C(NH2)3 = guanidinium). *Chem. Eur. J.* **2009**, *15*, 12050–12064. [[CrossRef](#)] [[PubMed](#)]
23. Rogez, G.; Viart, N.; Drillon, M. Multiferroic materials: The attractive approach of metal-organic frameworks (MOFs). *Angew. Chem. Int. Ed.* **2010**, *49*, 1921–1923. [[CrossRef](#)] [[PubMed](#)]
24. Pato-Doldán, B.; Gómez-Aguirre, L.C.; Bermúdez-García, J.M.; Sánchez-Andújar, M.; Fondado, A.; Mira, J.; Castro-García, S.; Señaris-Rodríguez, M.A. Coexistence of magnetic and electrical order in the new perovskite-like (C3N2H5)[Mn(HCOO)3] formate. *RSC Adv.* **2013**, *3*, 22404–22411. [[CrossRef](#)]
25. Gómez-Aguirre, L.C.; Pato-Doldán, B.; Mira, J.; Castro-García, S.; Señaris-Rodríguez, M.A.; Sánchez-Andújar, M.; Singleton, J.; Zapf, V.S.; Señaris-Rodríguez, M.A.; Sánchez-Andújar, M.; et al. Magnetic Ordering-Induced Multiferroic Behavior in [CH3NH3][Co(HCOO)3] Metal-Organic Framework. *J. Am. Chem. Soc.* **2016**, *138*, 1122–1125. [[CrossRef](#)] [[PubMed](#)]
26. Li, W.; Stroppa, A.; Wang, Z.; Gao, S. *Hybrid Organic-Inorganic Perovskites*; Wiley-VCH Verlag: Weinheim, Germany, 2020; ISBN 978-3-527-34431-4.
27. Baraldi, P. Thermal behaviour of metal carboxylates: Metal formates. *Spectrochim. Acta Part A Mol. Spectrosc.* **1979**, *35*, 1003–1007. [[CrossRef](#)]
28. Dollimore, D.; Tonge, K.H. The thermal decomposition of zinc and manganese formates. *J. Inorg. Nucl. Chem.* **1967**, *29*, 621–627. [[CrossRef](#)]
29. Dollimore, D.; Gupta, J.P.; Nowell, D.V. The thermal decomposition of metal formates. II. Solid state thermal decomposition studies on magnesium formate dihydrate. *Thermochim. Acta* **1979**, *30*, 339–350. [[CrossRef](#)]
30. Rozenberg, A.S.; Aleksandrova, E.I. Thermal decomposition of transition metal carboxylates: 1. Decomposition of anhydrous copper(II) formate. Morphology and regularities of gas evolution. *Russ. Chem. Bull.* **1996**, *45*, 64–68. [[CrossRef](#)]
31. NIST Chemistry WebBook. Available online: [webbook.nist.gov/chemistry/](http://webbook.nist.gov/chemistry/) (accessed on 14 April 2020).
32. Shishido, S.; Masuda, Y. The Gaseous Products formed in the Thermal Decompositions of Formates. *Nippon Kagaku Kaishi* **1973**, *1973*, 185–188. [[CrossRef](#)]
33. Małecka, B.; Łącz, A. Thermal decomposition of cadmium formate in inert and oxidative atmosphere. *Thermochim. Acta* **2008**, *479*, 12–16. [[CrossRef](#)]
34. McBreen, P.H.; Serghini-Monim, S.; Roy, D.; Adnot, A. Decomposition of formic acid on FeTi. *Surf. Sci.* **1988**, *195*. [[CrossRef](#)]
35. Das, R.; Pachfule, P.; Banerjee, R.; Poddar, P. Metal and Metal Oxide Nanoparticle Synthesis from Metal Organic Frameworks (MOFs): Finding the Border of Metal and Metal Oxides. *Nanoscale* **2012**, *4*, 591–599. [[CrossRef](#)] [[PubMed](#)]
36. Gómez-Aguirre, L.C.; Pato-Doldán, B.; Stroppa, A.; Yáñez-Vilar, S.; Bayarjargal, L.; Winkler, B.; Castro-García, S.; Mira, J.; Sánchez-Andújar, M.; Señaris-Rodríguez, M.A. Room-Temperature Polar Order in [NH4][Cd(HCOO)3]—A Hybrid Inorganic–Organic Compound with a Unique Perovskite Architecture. *Inorg. Chem.* **2015**, *54*, 2109–2116. [[CrossRef](#)] [[PubMed](#)]
37. Sasaki, S.; Takeuchi, Y.; Fujino, K. X-Ray Determination of Electron-Density Distributions in Oxides, MgO, MnO, CoO, and NiO, and Atomic Scattering Factors of their Constituent Atoms. *Proc. Jpn. Acad. Ser. B Phys. Biol. Sci.* **1979**, *55*, 43–48. [[CrossRef](#)]
38. Kihara, K.; Donnay, G. Anharmonic thermal vibrations in ZnO. *Can. Mineral.* **1985**, *23*, 647–654.

39. Owen, E.A.; Yates, E.L. LXVI. X-ray measurement of the thermal expansion of pure nickel. *Lond. Edinb. Dublin Philos. Mag. J. Sci.* **1936**, *21*, 809–819. [[CrossRef](#)]
40. Rutt, O.J.; Williams, G.R.; Clarke, S.J. Reversible lithium insertion and copper extrusion in layered oxysulfides. *Chem. Commun.* **2006**, 2869–2871. [[CrossRef](#)] [[PubMed](#)]
41. Wyckoff, R.W.G. Cubic closest packed, ccp. *Struct. Cryst. Struct.* **1963**, *1*, 33.
42. Viertelhaus, M.; Anson, C.E.; Powell, A.K. Solvothermal synthesis and crystal structure of one-dimensional chains of anhydrous zinc and magnesium formate. *Zeitschrift Anorg. Allg. Chemie* **2005**, *631*, 2365–2370. [[CrossRef](#)]
43. Viertelhaus, M.; Henke, H.; Anson, C.E.; Powell, A.K. Solvothermal synthesis and structure of anhydrous manganese(II) formate, and its topotactic dehydration from manganese(II) formate dihydrate. *Eur. J. Inorg. Chem.* **2003**, *2003*, 2283–2289. [[CrossRef](#)]
44. Zachariasen, W.H. Untersuchungen über die Kristallstruktur von Sesquioxiden und Verbindungen ABO<sub>3</sub>. In *Proceedings of the Skrifter Utgitt av Det Norske Videnskaps-Akademi i Oslo 1: Matematisk- Naturvidenskapelig Klasse; i kommisjon HJ Dybwad; Det Norske Videnskaps-Akademi: Oslo, Norway*, 1928.
45. Walmsley, H.P. The structure of the smoke particles from a cadmium arc. *Proc. Phys. Soc.* **1927**, *40*, 7. [[CrossRef](#)]
46. Post, M.L.; Trotter, J. Cadmium(II) formate dihydrate. *Acta Crystallogr. Sect. B* **1974**, *30*, 1880–1882. [[CrossRef](#)]
47. Weber, G. The structure of anhydrous cadmium formate. *Acta Crystallogr. Sect. B Struct. Crystallogr. Cryst. Chem.* **1980**, *36*, 1947–1949. [[CrossRef](#)]
48. Graulis, S.; Chateigner, D.; Downs, R.T.; Yokochi, A.F.T.; Quirós, M.; Lutterotti, L.; Manakova, E.; Butkus, J.; Moeck, P.; Le Bail, A. Crystallography Open Database—An open-access collection of crystal structures. *J. Appl. Crystallogr.* **2009**, *42*, 726–729. [[CrossRef](#)] [[PubMed](#)]
49. Downs, R.T.; Hall-Wallace, M. The American Mineralogist crystal structure database. *Am. Mineral.* **2003**, *88*, 247–250.
50. Linstrom, P.; Mallard, W. The NIST Chemistry WebBook: A Chemical Data Resource on the Internet. *J. Chem. Eng. Data* **2001**, *46*, 1059–1063. [[CrossRef](#)]